

## Size distributions of nanoscopic holes in Ti/*h*-BN and Ti/B nanocomposites

J. Čížek,<sup>1,a)</sup> I. Procházka,<sup>1</sup> O. S. Morozova,<sup>2</sup> C. Borchers,<sup>3</sup> and A. Pundt<sup>3</sup>

<sup>1</sup>Faculty of Mathematics and Physics, Charles University, Prague, V Holešovičkách 2, CZ-18000 Praha 8, Czech Republic

<sup>2</sup>Semenov Institute of Chemical Physics, RAS, Kosygin st. 4, 119991 Moscow, Russia

<sup>3</sup>Institut für Materialphysik, Universität Göttingen, Friedrich-Hund-Platz 1, D-37077 Göttingen, Germany

(Received 3 August 2009; accepted 6 January 2010; published online 19 February 2010)

Positron annihilation spectroscopy was employed for defect studies of “Ti”-based nanocomposites prepared by high-energy ball milling and consisting of Ti nanoparticles separated by hexagonal boron nitride (*h*-BN) or boron (B) additive. The size distribution of nanoscopic holes in nanocomposites was determined directly from measurement of ortho-positronium (Ps) lifetimes. Chemical environment of defects was characterized using coincidence Doppler broadening. It was found that size of nanoscopic holes is reduced with increasing milling time in H<sub>2</sub>/He atmosphere and also probability of Ps formation in holes decreases. At the same time the Ti content in the vicinity of holes increases. This can be explained by (i) increased intermixing of Ti particles with *h*-BN or B additive and by (ii) filling the nanoscopic holes with absorbed hydrogen. Analysis of obtained results showed that both these processes take place during milling of nanocomposites. In addition, it was found that the effect of filling the nanoscopic pores with hydrogen is enhanced in TiH<sub>2</sub> milled with *h*-BN or B in He atmosphere. Comparison of nanocomposites with *h*-BN and B additive showed that sufficiently long milling time leads to a similar size distribution of nanoscopic holes in Ti/*h*-BN and Ti/B, despite the fact that it differs substantially in the initial powders. However, density of nanoscopic holes in Ti/B is significantly lower than in Ti/*h*-BN nanocomposites. © 2010 American Institute of Physics. [doi:10.1063/1.3305790]

### I. INTRODUCTION

Titanium is widely used as an ingredient of hydrogen storage materials. Titanium hydride (TiH<sub>2</sub>) can be prepared from “Ti” and H<sub>2</sub> during reactive milling.<sup>1,2</sup> However, a major drawback of Ti-based hydrides is a high working temperature and sluggish sorption kinetics. The poor kinetic properties are improved in nanocrystalline materials with a high volume fraction of grain boundaries. The improvement in hydrogen kinetics in nanocrystalline Ti powders is caused by two main factors: (i) enhanced hydrogen diffusivity due to high surface area of nanoparticles or due to diffusion along grain boundaries<sup>3</sup> and (ii) addition of catalyzing substances, which are finely dispersed in a nanocomposite material and which increase sorption kinetics of the hydride phase.<sup>4</sup> Nanocrystalline Ti powders with a high concentration of grain boundaries can be produced by high-energy ball milling,<sup>5,6</sup> which enables to achieve a uniform spread of a suitable catalyst and its close contact with the metal. It was found that addition of graphite considerably accelerates and increases hydrogen uptake into Ti.<sup>7–9</sup> Recently it has been demonstrated that hexagonal boron nitride (*h*-BN) is even more efficient additive.<sup>10</sup> The total hydrogen uptake of Ti/*h*-BN nanocomposites amounts to 0.84 H/Ti whereby 55% of absorbed hydrogen atoms occupy low-temperature desorption sites.<sup>10</sup>

The Ti/*h*-BN nanocomposite represents a rather complicated system where active Ti nanoparticles are separated by a microporous *h*-BN matrix, which prevents their agglomera-

tion. Nanostructured *h*-BN matrix may contain small pores with size ranging from a few angstrom up to hundreds angstrom. Hence, concentration and size distribution of nanoscopic holes in *h*-BN are important parameters in design of Ti/*h*-BN nanocomposites for hydrogen storage. There is still a lack of information about the size distribution of these nanoscopic pores and also about possible filling of these holes by hydrogen. In the present work we studied the size distribution of nanoscopic holes in *h*-BN powder and Ti/*h*-BN nanocomposites. For comparison characterization of nanoscopic pores were performed also in Ti/B nanocomposites, i.e., Ti nanoparticles separated by boron. The influence of hydrogen on the distribution of nanoscopic pores was investigated both in Ti/*h*-BN and Ti/B nanocomposites.

Positron annihilation spectroscopy (PAS) was employed to obtain direct information about size distribution and concentration of nanoscopic holes. PAS is a well developed technique for the characterization of open volume defects (e.g., vacancies, dislocations, voids, etc.) on the atomic scale.<sup>11</sup> Measurement of positron lifetime (PL) enables to identify open-volume defects in studied sample and also to determine defect densities.

Typical kinetic energy of a positron emitted by a radioactive nucleus is in order of 10<sup>2</sup> keV. A fast positron injected into a solid loses quickly its kinetic energy by ionizing the host atoms and creating a spur of free electrons on its slowing-down path. A thermalized positron may couple with an electron in the spur and form positronium (Ps),<sup>12</sup> i.e., a hydrogenlike binding state of a positron and an electron. One can distinguish between singlet para-Ps (p-Ps) and triplet ortho-Ps (o-Ps) states which are formed in the ratio 1:3.<sup>13</sup>

<sup>a)</sup>Electronic mail: jakub.cizek@mff.cuni.cz.

Spin exchange repulsion between the electron bound to positron and core electrons and Coulomb repulsion between positron and ions repel Ps and push it into interstitial regions. However, electron density in interstitial regions in most of crystalline solids is still relatively high and Ps is quickly destroyed due to interaction with other electrons. However, if the material contains open volume defects (voids, pores), which are large enough, then Ps may be trapped at these defects. Hence, a Ps atom having a size of about 1.59 Å is an ideal probe of nanoscopic pores. The p-Ps where electron and positron have opposite spin decays quickly via self-annihilation—the lifetime of p-Ps in vacuum is 0.125 ns only.<sup>13</sup> On the other hand, self-annihilation rate of o-Ps is roughly three orders of magnitude lower compared to p-Ps and the lifetime of o-Ps in vacuum is 142 ns.<sup>13</sup> In solids o-Ps may annihilate with an electron of opposite spin from the surrounding media. This so-called pick-off annihilation significantly shortens lifetime of o-Ps in solids typically down to a few nanoseconds. The probability of pick-off annihilation of a Ps localized in an open-volume defect is determined by overlap of its wave function with wave functions of surrounding electrons, i.e., on the overlap of Ps with the walls of the hole. Obviously this overlap and, thereby, the probability of pick-off annihilation increases with decreasing size of defect. Hence, o-Ps lifetime depends on the size of the hole. Tao<sup>14</sup> and Eldrup *et al.*<sup>15</sup> proposed a semi-empirical equation, which relates the o-Ps lifetime  $\tau_{o\text{-Ps}}$  with the radius  $R$  of a spherical open volume hole

$$\tau_{o\text{-Ps}} = \frac{1}{2} \left[ 1 - \frac{R}{R + \Delta R} + \frac{1}{2\pi} \sin\left(\frac{2\pi R}{R + \Delta R}\right) \right]^{-1}. \quad (1)$$

The parameter  $\Delta R = 1.66 \text{ \AA}$  represents the depth of penetration of the Ps wave function into the walls of the holes and was determined by fitting the model to a number of materials containing nanoscopic open volume holes of known size.<sup>16</sup> Equation (1) enables to determine the average radius  $R$  of a spherical open volume hole from o-Ps lifetime measured in experiment. One can deduce from Eq. (1) that the diameter of open volume hole must exceed at least  $2\Delta R \approx 3 \text{ \AA}$  to confine Ps. Hence, the term nanoscopic hole used in this paper means open volume defect (pore), which can be considered as a Ps trap, i.e., with size exceeding  $3 \text{ \AA}$ . In principle there is no upper limit on size of pores detectable by Ps, however, for pores so large that the probability of pick-off annihilation becomes negligible, the o-Ps lifetime changes with pore size are not measurable anymore.

## II. EXPERIMENTAL DETAILS

### A. Sample preparation

The initial ingredients were Ti (99.5%) powder consisting of spherical particles of about 200  $\mu\text{m}$  in diameter and *h*-BN ( $\sim 99\%$ ) powder with mean particle size of 4  $\mu\text{m}$  or crystalline B (99%) powder with particle size around 10  $\mu\text{m}$ . Two kinds of specimens were investigated in this work:

- (i) Ti/*h*-BN nanocomposites prepared by milling of the initial Ti powder with *h*-BN and

TABLE I. Composition and parameters of mechanical-chemical treatment of Ti/*h*-BN and Ti/B nanocomposites.

Sample	Powder composition	Milling time interval (min)	Effluent gas
Ti/ <i>h</i> -BN nanocomposites			
TiH <sub>2</sub> / <i>h</i> -BN	1.5g TiH <sub>2</sub> +0.3g <i>h</i> -BN	66	He
Ti/ <i>h</i> -BN-1	1.5g Ti+0.3g <i>h</i> -BN	66	50%H <sub>2</sub> +50%He
Ti/ <i>h</i> -BN-2	1.5g Ti+0.3g <i>h</i> -BN	206	50%H <sub>2</sub> +50%He
Ti/B nanocomposites			
TiH <sub>2</sub> /B	1.5g TiH <sub>2</sub> +0.3g <i>h</i> -B	66	He
Ti/B-1	1.5g Ti+0.3g <i>h</i> -B	66	50%H <sub>2</sub> +50%He
Ti/B-2	1.5g Ti+0.3g <i>h</i> -B	206	50%H <sub>2</sub> +50%He

- (ii) Ti/B nanocomposites prepared by milling of the initial Ti powder with B.

The fraction of *h*-BN or B additive was in all cases 16.7 wt %, which corresponds to 47 at. % for B and 44 at. % for *h*-BN. Hydrating experiments were carried out under flow conditions in a flow mechanical-chemical reactor fixed to the vibrator. The following parameters were used for the milling process: a stainless-steel container was loaded with 1.8 g of Ti/*h*-BN or Ti/B reaction mixture together with 19.8 g hardened steel balls (diameter 3–5 mm); the vibration frequency was 50 Hz with an amplitude of milling of 7.25 mm, and the average energy intensity of 1.0 W/g. The effluent gas composition was monitored continuously by a gas chromatograph combined online with the milling device. The time interval of milling and the composition of effluent gas used in the milling treatment of various specimens are listed in Table I. The chemical state and local electronic structure of Ti and N atoms were studied by soft x-ray emission spectroscopy (XES) and the results have been published recently in Ref. 10.

### B. PAS

A <sup>22</sup>Na<sub>2</sub>CO<sub>3</sub> positron source with an activity of 1.5 MBq deposited on a 2  $\mu\text{m}$  thick mylar foil was used in PAS measurements. The source was placed in the center of a small cylindrical chamber with a diameter of 8 mm and height of 5 mm. Subsequently, the chamber was completely filled with the measured powder and closed. Dimensions of the chamber ensure that virtually all positrons are thermalized inside the chamber and, thereby, annihilate in the studied powder.

PL measurements were performed on a digital PL spectrometer described in Refs. 17 and 18. The spectrometer is equipped with BaF<sub>2</sub> scintillators and fast photomultipliers Hamamatsu H3378. Detector pulses are directly digitized using a couple of 8-bit ultrafast digitizers Acqiris DC 211 with sampling frequency of 4 GHz and stored in a personal computer (PC). Analysis of digitized pulses and construction of PL spectrum is performed off-line using so-called integral true constant fraction technique described in Ref. 19. The spectrometer exhibits excellent timing resolution of 145 ps (full width at half maximum <sup>22</sup>Na). The PL spectra, which always contained at least 10<sup>7</sup> positron annihilation events, were decomposed using a least square fitting program LT

(version 9) described in Ref. 20. The source contribution to PL spectra consisted of two weak components with lifetimes of approximately 368 ps and 1.5 ns and corresponding intensities of approximately 8% and 1%.

Coincidence Doppler broadening (CDB) studies were carried out using a spectrometer<sup>21</sup> equipped with two high purity Ge detectors. The energy resolution of the CDB spectrometer is  $(1.02 \pm 0.01)$  keV at 511 keV. At least  $10^8$  annihilation events were collected in each two-dimensional  $\gamma$ -ray energy spectrum, which was subsequently reduced into two one-dimensional cuts representing the resolution function of spectrometer and Doppler broadened annihilation profile. In this paper CDB results are presented as ratio curves with respect to the initial *h*-BN powder. A well annealed bulk Ti (99.95%) specimen was used to determine shape of a pure contribution of positrons annihilated by Ti electrons.

### C. Theoretical calculations of positron parameters

Positron parameters were calculated from first principles using an approach based on the density functional theory. Calculations of positron density were performed within so-called conventional scheme employing the atomic superposition (ATSUP) method.<sup>22</sup> Electron-positron correlation was treated using the scheme developed by Boronski and Nieminen<sup>23</sup> with the correction<sup>24</sup> for incomplete positron screening with high frequency dielectric constants  $\epsilon_\infty=4.5$  (Ref. 25) and 8.77 (Ref. 26) for *h*-BN and B, respectively. A closed packed hexagonal structure with lattice parameters  $a=2.9508$  Å,  $c=4.6855$  Å (Ref. 27) was assumed for Ti. Theoretical calculations for *h*-BN were performed for hexagonal graphitelike structure with lattice parameters  $a=2.054$  Å and  $c=6.661$  Å.<sup>28</sup> Rhombohedral structure with lattice parameters  $a=5.06$  Å,  $\alpha=58.060^\circ$  (Ref. 29) was assumed for  $\alpha$ -B. A supercell approach was used for positrons trapped at vacancies. The calculations for Ti and *h*-BN were performed using 512 atom-based supercells, while 768 atom-based supercells were used for B. Vacancies were created simply by removing the appropriate number of atoms from the supercell.

## III. RESULTS AND DISCUSSION

### A. Reference Ti specimen

Calculated lifetimes of free positrons and positrons trapped in Ti vacancy are listed in Table II, while Table III shows results of PL measurements. The well annealed Ti specimen exhibits a single component PL spectrum with life-

TABLE II. Calculated bulk PLs, lifetimes of positrons trapped at vacancies, and positron binding energies  $E_B$  to vacancies in the studied materials. PLs published in literature are shown in the last column.

	Present work		Literature
	$\tau$ (ps)	$E_B$ (eV)	$\tau$ (ps)
Ti-bulk	147	...	147 [30]
Ti-vacancy	237	5.5	236 [30]
<i>h</i> -BN-bulk	330	...	
<i>h</i> -BN-vacancy(B)	336	<0.1	
<i>h</i> -BN-vacancy(N)	334	<0.1	
$\alpha$ -B-bulk	154	...	
$\alpha$ -B-vacancy	163	0.14	

time  $\tau_B$ , which agrees well with the calculated lifetime of free positrons in a perfect Ti crystal, see Table II and also Ref. 30. Hence, defect density in well annealed Ti specimen is very low (below the detection limit of PL spectroscopy) and the specimen can be considered as a defect-free material.

### B. *h*-BN and B initial powders

Figure 1 shows PL spectra (with subtracted background and normalized to the same area) for pure *h*-BN and B powders. One can clearly see in the figure that PL spectrum of *h*-BN powder exhibits significantly longer components compared to PL spectrum of B powder. In particular, very long component originating from o-Ps annihilations can be clearly seen in PL spectrum of *h*-BN but it is absent in the PL spectrum of B powder.

It was found that B powder exhibits only a single component PL spectrum (except of the source contribution)

$$S(t) = \frac{1}{\tau_d} e^{-t/\tau_d}, \quad (2)$$

with lifetime  $\tau_d \approx 194$  ps, see Table III. This testifies that virtually all positrons in the sample annihilate from a single state. The experimental lifetime  $\tau_d$  is remarkably longer than calculated bulk PL in B and even longer than the lifetime of positrons trapped at monovacancy in B, see Table II. This indicates that B powder contains open volume defects larger than monovacancies. Calculated lifetimes of positrons trapped at various vacancy clusters in B are plotted in Fig. 2 as a function cluster diameter  $d$  estimated as

TABLE III. Results of PL measurements of the studied materials in the initial state.

	$\tau_f$ (ps)	$I_f$ (%)	$\tau_d$ (ps)	$I_d$ (%)	$\tau_{o-Ps}$ (ns)	$\sigma_{o-Ps}$ (ns)	$I_{Ps}$ (%)
Ti bulk	146.1(5)	100					
Well annealed							
B	194.4(2)	100					
Powder							
<i>h</i> -BN	182(3)	17.7(6)	391(3)	59.5(5)	2.01(2)	0.65(3)	22.8(3)
Powder							

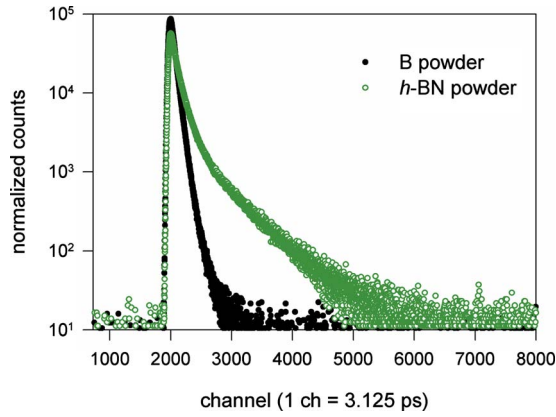


FIG. 1. (Color online) PL spectra (normalized to the same area and with subtracted background) of B and *h*-BN powder.

$$d = \sqrt[3]{nd_B}, \quad (3)$$

where  $n$  is the number of vacancies in the cluster and  $d_B \approx 1.62$  Å is distance of nearest neighbor atoms in B lattice. Clearly the lifetime of trapped positrons increases with increasing size of clusters. The lifetime determined experimentally in initial B powder, see Table III, is comparable with the lifetime calculated for positrons trapped at divacancies in B. Note that even longer PL of  $(243 \pm 5)$  ps was measured on commercial B powder in Ref. 31. Unfortunately no details about this powder were mentioned. However, it is likely that the B powder investigated in Ref. 31 contains larger vacancy clusters than the B powder studied in this work. However, the absence of a Ps component in the PL spectrum of the initial B powder indicates that it does not contain nanoscopic pores. Nevertheless, it should be mentioned that in some materials formation of Ps may be inhibited even if they contain nanoscopic pores. This occurs usually in materials containing free radicals which catch free electrons created in the spur.<sup>32</sup> As a consequence, free electrons are not available for formation of Ps. Moreover, o-Ps may also undergo a spin conversion to p-Ps when it collides with paramagnetic molecules.<sup>33</sup> This effect reduces significantly the lifetime of o-Ps and increases intensity of short-lived p-Ps component. As the B powder does contain neither free radicals nor paramagnetic molecules and short-lived p-Ps component was not detected in the PL spectrum we may conclude that the ab-

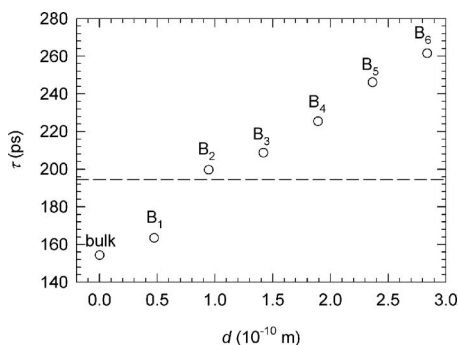


FIG. 2. Calculated lifetimes of positrons trapped at various vacancy clusters in B as a function cluster diameter  $d$ . The symbol  $B_n$  denotes a cluster consisting of  $n$  vacancies. The lifetime measured on initial B powder is shown by a dashed line.

sence of Ps component testifies that the initial B powder does not contain nanoscopic pores.

The PL spectrum of *h*-BN powder is more complicated. It contains a contribution of positrons annihilating from the free state and also from the localized state at defects. In addition, it contains also a contribution of Ps annihilations. Hence, the PL spectrum  $S(t)$  was fitted using the model

$$S(t) = \frac{I_f}{\tau_f} e^{-t/\tau_f} + \frac{I_d}{\tau_d} e^{-t/\tau_d} + \frac{1}{4} I_{Ps} \frac{1}{\tau_{p-Ps}} e^{-t/\tau_{p-Ps}} + \frac{3}{4} I_{Ps} \int_0^\infty \lambda \alpha(\lambda) e^{-\lambda t} d\lambda, \quad (4)$$

where the first two terms represent contribution of positron annihilations, while the two last terms come from Ps annihilations. The parameters related to annihilation of positrons (lifetimes and intensities) are plotted in Figs. 3(a) and 3(b). The symbols  $\tau_f$  and  $\tau_d$ , respectively, denote the lifetime of free positrons and positrons trapped at defects. Relative intensities of positron components are denoted  $I_f$  and  $I_d$ , while  $I_{Ps}$  is the relative intensity of the Ps contribution. Note that intensities are normalized so that  $I_f + I_d + I_{Ps} = 100\%$ .

The p-Ps lifetime was fixed at  $\tau_{p-Ps} = 125$  ps in fitting of PL spectra. Annihilation of o-Ps is dominated by the pick-off process and the o-Ps lifetime reflects the size of nanoscopic holes in the specimen. It is assumed that the sample contains certain distribution  $H(R)$  of sizes of nanoscopic pores. This leads to a distribution of o-Ps lifetime, which is related to diameter  $R$  of a nanoscopic pore by Eq. (1).

The symbol  $\alpha(\lambda)$  in Eq. (4) denotes the distribution (probability density function) of o-Ps annihilation rates ( $\lambda = \tau_{o-Ps}^{-1}$ ) due to size distribution of nanoscopic holes. It was shown with the help of simulated spectra that the exact shape of  $\alpha(\lambda)$  cannot be determined because of statistical

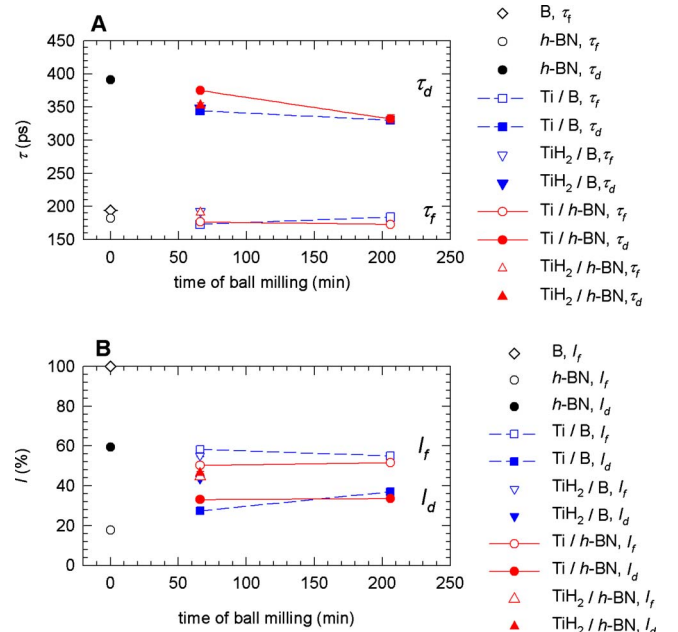


FIG. 3. (Color online) Parameters related to positron annihilations in Ti/*h*-BN and Ti/B nanocomposites plotted as a function of time of ball milling. Results for initial *h*-BN and B powder are shown in the figure as well. (a) PLs and (b) relative intensities.

uncertainties.<sup>34</sup> However, there is a possibility to determine the first two moments of  $\alpha(\lambda)$ , i.e., the mean value of  $\lambda$ , and its standard deviation. The fitting program LT (Ref. 20) employed in this work assumes that a complex component representing in PL spectrum a continuous sum of decay curves arising from the size distribution of nanoscopic holes can be approximated by a Gaussian distribution in a logarithmic scale of lifetimes. Here  $\lambda_0^{-1}$  and  $\sigma_0$  denote the expected mean value and standard deviation of the Gaussian distribution. Under this assumption the probability density function  $\alpha(\lambda)$  of annihilation rates is characterized by a log-normal distribution

$$\alpha(\lambda) = \frac{1}{\sigma_0 \sqrt{2\pi} \lambda} \exp\left[-\frac{(\ln \lambda - \ln \lambda_0)^2}{2\sigma_0^2}\right], \quad (5)$$

with its maximum at  $\lambda_0$ . The expected (mean) value of o-Ps lifetime is obtained from  $\alpha(\lambda)$  as

$$\tau_{\text{o-Ps}} = \int_0^\infty \frac{1}{\lambda} \alpha(\lambda) d\lambda = \frac{1}{\lambda_0} \exp \frac{\sigma_0^2}{2}. \quad (6)$$

The standard deviation  $\sigma_{\text{o-Ps}}$  of the o-Ps lifetime is given by the expression

$$\sigma_{\text{o-Ps}}^2 = \int_0^\infty \left(\frac{1}{\lambda} - \tau_{\text{o-Ps}}\right)^2 \alpha(\lambda) d\lambda = \frac{1}{\lambda_0^2} (e^{\sigma_0^2} - 1). \quad (7)$$

The parameters  $\tau_{\text{o-Ps}}$ ,  $\sigma_{\text{o-Ps}}$ , and  $I_{\text{Ps}}$  obtained from fitting of PL spectra are shown in Figs. 4(a)–4(c).

Comparison of experimental data with theoretical calculations shows that the lifetime  $\tau_f$  lies well below the calculated bulk lifetime  $\tau_B$  for a perfect (defect-free) *h*-BN crystal, while the lifetime  $\tau_d$  is longer. This is in agreement with the assignment of the shorter component to free positrons and the longer one to positrons trapped at defects. Consistency of a decomposition of PL spectrum with the simple trapping model (STM) (Ref. 35) can be checked using the well known identity

$$\tau_B \equiv (I_f + I_d) \left( \frac{I_f}{\tau_f} + \frac{I_d}{\tau_d} \right)^{-1}, \quad (8)$$

which holds in the frame of STM. Note that multiplication by the sum of intensities  $I_f + I_d$  in Eq. (8) is due to renormalization of intensities of the components originating purely from positrons (not from Ps). The right side of the Eq. (8) calculated from the experimental data measured on *h*-BN powder is  $(310 \pm 8)$  ps. This is in a reasonable agreement with the calculated bulk PL for a perfect *h*-BN crystal given in Table II.

The experimental lifetime  $\tau_d$  is longer than calculated lifetimes of positrons trapped at B- and N-vacancy in *h*-BN, see Table II. This indicates that similarly to the B powder, also the initial *h*-BN powder contains vacancy clusters which trap positrons. In order to identify these clusters, the experimental lifetime  $\tau_d$  was compared with lifetimes calculated for various vacancy clusters in *h*-BN, which are plotted in Fig. 5 as a function of the cluster diameter. Note that effective diameter  $d$  of a cluster consisting of  $n_B$  B-vacancies and  $n_N$  N-vacancies was estimated as

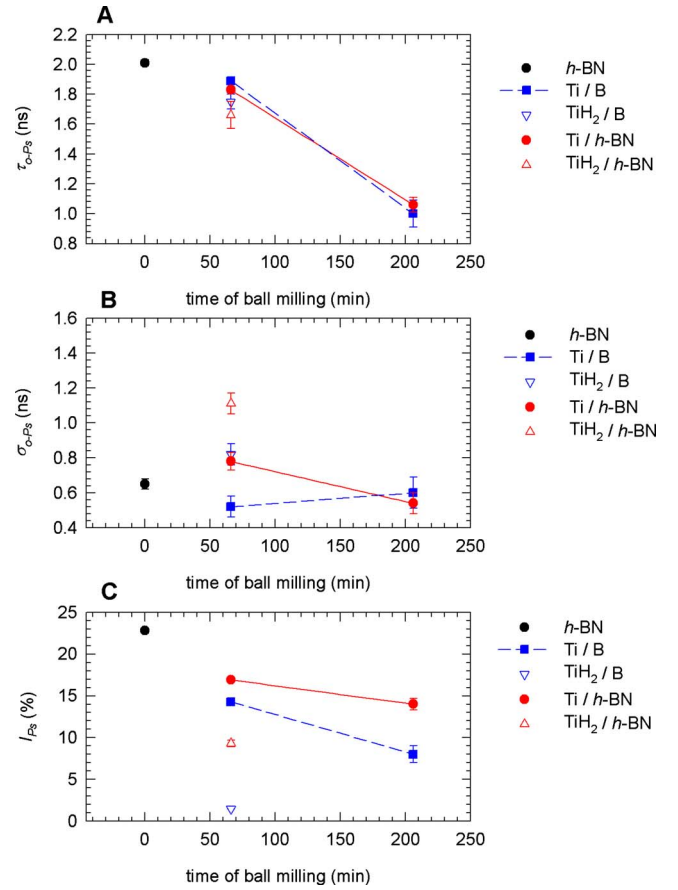


FIG. 4. (Color online) Parameters of the Ps component (a) o-Ps lifetime  $\tau_{\text{o-Ps}}$ , (b) dispersion of the o-Ps lifetime  $\sigma_{\text{o-Ps}}$ , and (c) intensity of the Ps component as a function of time of ball milling.

$$d = \sqrt[3]{n_B d_{\text{BN,B}}^3 + n_N d_{\text{BN,N}}^3}, \quad (9)$$

where  $d_{\text{BN,B}}$  and  $d_{\text{BN,N}}$  are effective diameters of B and N atoms in *h*-BN crystal. These diameters were estimated as

$$d_{\text{BN,B}} = \frac{r_B a_0}{r_B + r_N}, \quad (10)$$

and

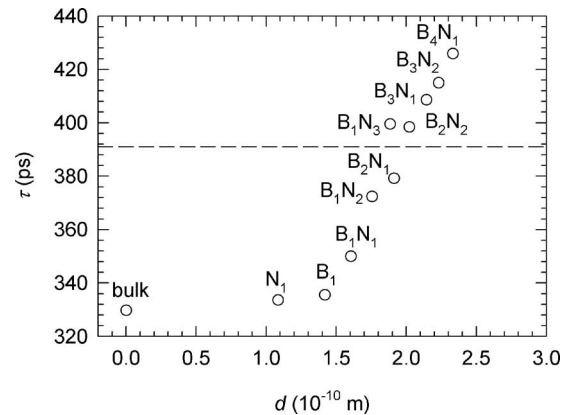


FIG. 5. Theoretically calculated lifetimes of positrons trapped at various vacancy clusters in *h*-BN as a function of vacancy cluster diameter estimated using Eqs. (9)–(11). The symbol  $B_x N_y$  denotes a vacancy cluster consisting of  $x$  B-vacancies and  $y$  N-vacancies. The experimental lifetime of positrons trapped at defects measured in pure *h*-BN powder is shown by a dashed line.

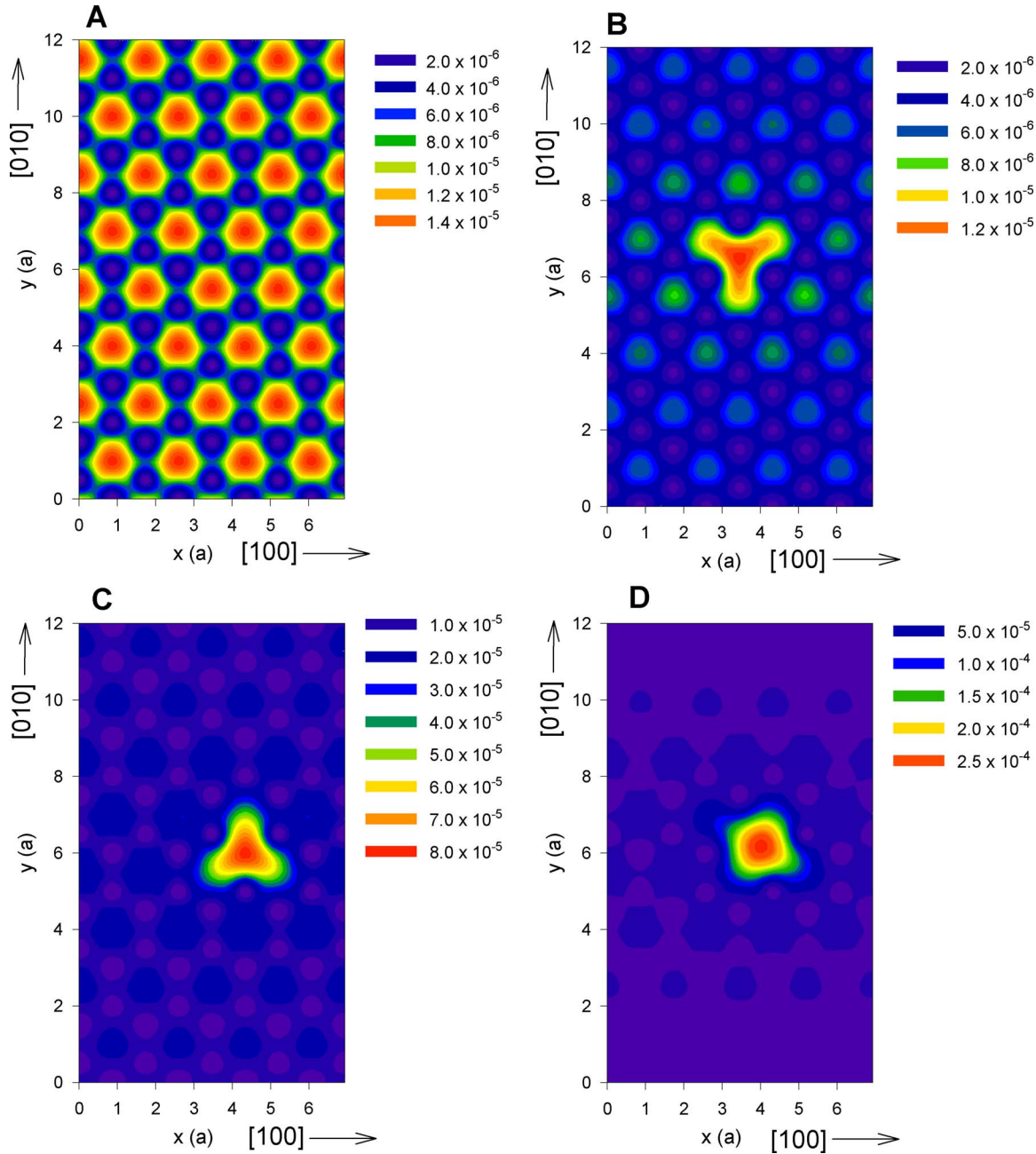


FIG. 6. (Color online) Calculated positron density in (0001) plane in *h*-BN crystal: (a) ideal crystal, (b) N-vacancy, (c) B-vacancy, and (d) BN-divacancy. Positron densities are plotted in atomic units. The distances are given in the units of *h*-BN lattice constant *a*.

$$d_{\text{BN},\text{N}} = \frac{r_{\text{N}}a_0}{r_{\text{B}} + r_{\text{N}}}. \quad (11)$$

Here  $r_{\text{B}}=0.85 \text{ \AA}$  and  $r_{\text{N}}=0.65 \text{ \AA}$  are neutral atom radii of B and N and  $a_0=2.504 \text{ \AA}$  is the distance of nearest neighbor atoms in *h*-BN crystal. Figure 5 shows that lifetime of trapped positrons remarkably increases with size of clusters and the experimental lifetime  $\tau_{\text{d}}$  is comparable with calculated lifetimes of positrons trapped in trivacancies or tetravacancies ( $\text{B}_2\text{N}_1$ ,  $\text{B}_2\text{N}_2$ , and  $\text{B}_3\text{N}_1$ ). Such small vacancy clusters are most probably formed during the preparation of the powder by agglomeration of monovacancies.

Note that from Fig. 5 and Table II it becomes clear that both B- and N-monovacancies in *h*-BN are only shallow positron traps incapable of complete localization of positron

wave function. This can be seen in Fig. 6 which compares positron density in (0001) plane in (A) a perfect *h*-BN crystal, (B) a crystal containing an N- and (C) a B-monovacancy. There is only a weak localization of positron in a B-monovacancy and even weaker in an N-monovacancy. This is due to the relatively open structure of *h*-BN with low average electron density in interatomic regions. More pronounced positron localization can be seen in a BN divacancy shown in Fig. 6(d). Therefore, the presence of monovacancies causes only a very slight increase in PL. Hence, one cannot exclude the existence of B- and N-monovacancies in the initial *h*-BN powder because monovacancies in *h*-BN are too shallow traps to be detected by positron annihilation at room temperature.

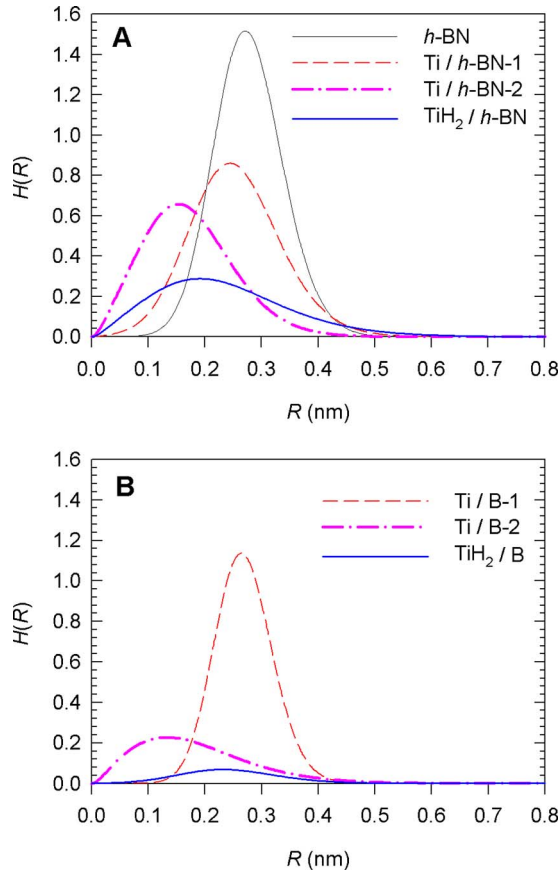


FIG. 7. (Color online) Size distribution  $H(R)$  of free volume radii normalized to  $I_{Ps}$  intensity according to Eq. (12) for (a) Ti/ $h$ -BN and (b) Ti/B nanocomposites. The nomenclature of nanocomposites used in the legend is the same as in Table I, i.e., Ti/ $h$ -BN-1 and Ti/ $h$ -BN-2 denote Ti/ $h$ -BN nanocomposites milled in  $H_2/He$  atmosphere for 66 and 206 min, respectively, while  $TiH_2/h$ -BN denotes  $TiH_2$  milled with  $h$ -BN additive for 66 min in pure He atmosphere.

It should be mentioned that Murakami and Endo<sup>36</sup> observed in  $h$ -BN powder a PL of  $(360 \pm 10)$  ps, which was attributed to positrons trapped at defects. This lifetime is comparable to our value and gives independent evidence that  $h$ -BN powder contains vacancy clusters.

Contrary to initial B powder,  $h$ -BN specimens exhibit a well separated long-lived o-Ps component, which testifies that  $h$ -BN powder contains nanoscopic porosity. The size distribution  $H(R)$  of nanoscopic pores in  $h$ -BN powder is plotted in Fig. 7(a) (thin black line). The distribution is normalized to the intensity of Ps component so that

$$\int_0^{\infty} H(R) dR = I_{Ps}. \quad (12)$$

Thus, the area of the distribution may be considered as a measure of concentration of the nanoscopic pores. This approximation holds under the assumption that Ps yield in the sample is not influenced by other factors, e.g., inhibition by free radicals<sup>32</sup> or quenching by paramagnetic species.<sup>33</sup> Here we assume that these effects may be neglected in B and  $h$ -BN and that variation in o-Ps yield in our samples is mainly due to variation in concentration of nanoscopic holes. The mean radius of nanoscopic pores in  $h$ -BN is  $R_{mean}$

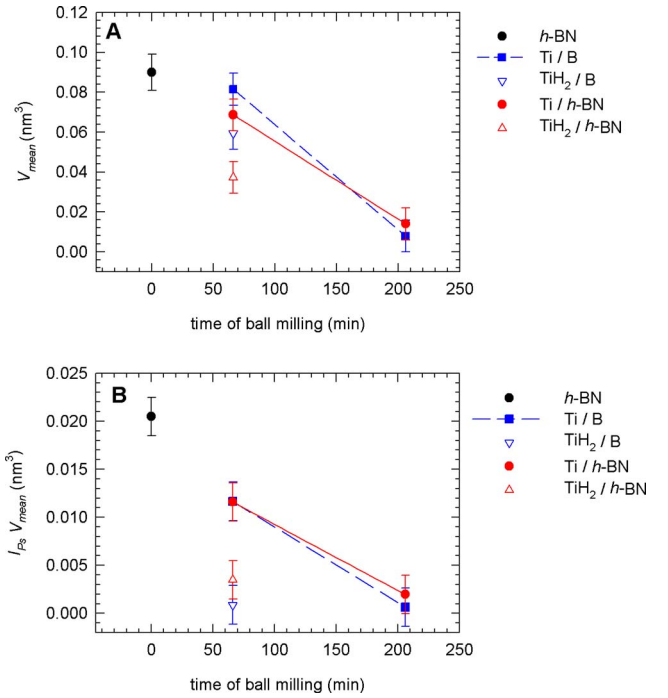


FIG. 8. (Color online) (a) Mean-free volume  $V_{mean}$  and (b) the quantity  $I_{Ps} V_{mean}$ , which is proportional to the volume occupied by porosity, see Eq. (15), plotted as a function of the milling time.

$= (0.28 \pm 0.01)$  nm, which corresponds to a mean-free volume of  $V_{mean} = (90 \pm 9) \times 10^{-3} \text{ nm}^3$ .

The difference between the volume of a unit mass of the powder  $V_{tot}$  and the reciprocal value of density  $\rho_{cryst}$  of a perfect  $h$ -BN crystal gives the volume  $V_f$  occupied by porosity

$$V_f = V_{tot} - \frac{1}{\rho_{cryst}}. \quad (13)$$

Free volume defined by Eq. (13) consists of (i) free space between powder grains  $V_{fo}$  and (ii) nanoscopic holes inside grains  $V_{fi}$

$$V_f = V_{fo} + V_{fi}. \quad (14)$$

As contribution of Ps annihilating in the free space between powder grains is too small to be detected, o-Ps component carries information about  $V_{fi}$ . In the simplest approximation  $V_{fi}$  is proportional to the product of the intensity of the Ps component and the mean-free volume of pores

$$V_{fi} \propto I_{Ps} V_{mean}. \quad (15)$$

Although this approximation has severe limitations already mentioned in the text, in particular, it does not take into account possible changes in the probability of o-Ps formation in various samples, the quantity  $I_{Ps} V_{mean}$ , which is plotted in Fig. 8, gives us a rough but useful estimation of trends in  $V_f$  in various samples.

### C. Ti/ $h$ -BN and Ti/B nanocomposites

Figure 9 shows PL spectra for initial  $h$ -BN powder and Ti/ $h$ -BN nanocomposites. One can clearly see in the figure that intensity of the long-lived o-Ps component gradually

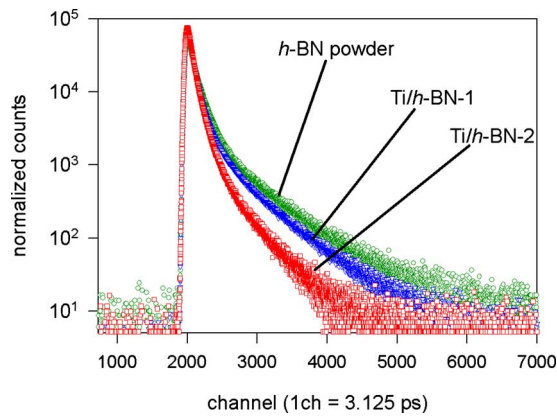


FIG. 9. (Color online) PL spectra (normalized to the same area and with subtracted background) of *h*-BN powder and Ti/*h*-BN nanocomposites. Ti/*h*-BN-1 denotes Ti milled with *h*-BN additive in H<sub>2</sub>/He atmosphere for 66, while Ti/*h*-BN-2 denotes the same nanocomposite but milled for 206 min.

decreases with increasing period of milling treatment. Similar effect was observed also in Ti/B nanocomposites

The PL spectra of *h*-BN powder and Ti/*h*-BN and Ti/B nanocomposites can be well fitted by Eq. (4). The parameters of positron contributions are shown in Fig. 3. In nanocomposites, the shorter component with lifetime  $\tau_f$  represents not only a contribution of free positrons annihilating in *h*-BN but also a contribution of positrons annihilating in Ti particles. The calculated lifetimes for Ti shown in Table II indicate that free positrons, as well as positrons trapped at Ti vacancies, should contribute to the shorter component. Because of statistical uncertainties, it is not possible to resolve all these contributions as individual components in PL spectra. Hence, the lifetime  $\tau_f$  of the shorter component resolved in nanocomposites represents an effective value which comes from all these contributions. A substantial increase in intensity  $I_f$  of the shorter component seen in Ti/*h*-BN and Ti/B nanocomposites in Fig. 3(b) is, therefore, caused by positrons annihilating in Ti particles.

The lifetime  $\tau_d$  of the longer component, which comes from positrons trapped in vacancy clusters, gradually decreases with increasing milling time in H<sub>2</sub>/He atmosphere, see Fig. 3(a). This is could be due to a decrease in cluster size, e.g., by splitting of clusters into smaller ones, during milling. Splitting of clusters leads to an increase in their density, which should be reflected by an increase in intensity  $I_d$ . A slight increase in  $I_d$  with milling time can be indeed observed in Ti/B nanocomposite. On the other hand, in Ti/*h*-BN  $I_d$  remains basically unchanged during milling, which does not correspond to splitting of clusters during milling. For this reason more probable explanation of the observed decrease in  $\tau_d$  with milling time could be filling of vacancy clusters in the nanocomposites with hydrogen, which enhances the local electron density in vacancy cluster and reduces, thereby, lifetime of trapped positrons. This explanation is supported by the fact that after prolonged milling of Ti/*h*-BN and Ti/B nanocomposite the lifetime  $\tau_d$  decreased approximately to a value observed in TiH<sub>2</sub>-based nanocomposites already after a shorter milling for 66 min. As discussed in the Sec. III D, hydrogen in TiH<sub>2</sub>-based nano-

composites is already embedded in the powder, which makes its diffusion to vacancy clusters easier and, thereby filling of vacancy clusters with hydrogen is expected to be faster in TiH<sub>2</sub>-based nanocomposites.

The parameters of the o-Ps component for Ti/*h*-BN and Ti/B nanocomposites are plotted in Figs. 4(a)–4(c). One can see in Fig. 4 A that all nanocomposites exhibit shorter o-Ps lifetime compared to initial *h*-BN powder. This testifies a decrease in size of nanoscopic pores, which can be seen as a shift in the maximum of the size distribution of  $H(R)$  plotted for Ti/*h*-BN nanocomposites in Fig. 7. Simultaneously the intensity of Ps component decreases with milling time, see Fig. 4(c). This occurs due to

- (i) filling of nanoscopic holes by hydrogen and/or
- (ii) increased intermixing of Ti and *h*-BN (or B) powders with increasing milling time.

The Ti/*h*-BN nanocomposite milled for 66 h exhibits larger dispersion of o-Ps lifetime than Ti/B sample milled for the same time. This is likely because of packing of atoms in *h*-BN structure is less tight than in B lattice. Hence, the Ti/*h*-BN nanocomposites may contain a larger variety of nanoscopic pores than the Ti/B nanocomposites. However, after prolonged ball milling for 206 min, the dispersions of the o-Ps component converge to similar value in both nanocomposites. This testifies that long milling causes formation of similar pores in Ti/*h*-BN and Ti/B nanocomposites despite the initial difference caused by different structures of the *h*-BN and B additives. One can see in Fig. 4(c) that Ti/B nanocomposites exhibit generally lower intensity of Ps component compared to Ti/*h*-BN samples, i.e., the o-Ps yield in Ti/B nanocomposites is lower than in Ti/*h*-BN. Hence, assuming that probability of Ps formation is determined predominantly by variations in number of holes, see discussion in Sec. III B, this result indicates that Ti/B nanocomposites contain lower concentration of nanoscopic holes compared to Ti/*h*-BN nanocomposites. This is likely due to closer packed structure of B compared to *h*-BN. This difference between Ti/*h*-BN and Ti/B nanocomposites remains even after prolonged milling.

CDB ratio curves (related to *h*-BN) for Ti/*h*-BN nanocomposites are shown in Fig. 10. Ratio curve for a well annealed bulk sample of pure Ti is plotted in the figure as well. One can see in Fig. 10 that CDB ratio curves of Ti/*h*-BN nanocomposites exhibit similar features as the curve of pure Ti reference sample indicating that some positrons are annihilated by Ti electrons. This contribution obviously increases with milling time testifying increased level of intermixing of Ti and *h*-BN particles. Nevertheless, the majority of positrons annihilate in the *h*-BN matrix. By comparison with CDB curve for a pure Ti one can estimate that roughly 15% of positrons annihilates inside Ti particles in Ti/*h*-BN nanocomposite milled for 66 min. Recent x-ray diffraction and transmission electron microscopy investigations of our nanocomposites<sup>37</sup> revealed that the Ti/*h*-BN nanocomposite milled for 66 min contains  $\alpha$ -Ti domains with mean size around 20 nm and also cubic  $\delta$ -TiH<sub>1.5-1.95</sub> particles with size around 10 nm embedded in *h*-BN matrix in grains with size around 100 nm. These grains form larger agglom-

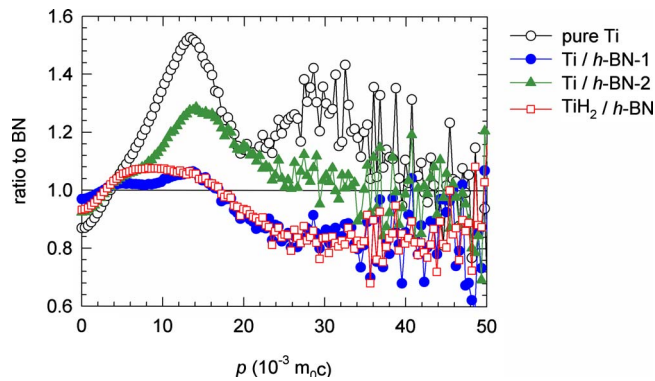


FIG. 10. (Color online) CDB ratio spectra (related to pure *h*-BN) for Ti/*h*-BN and TiH<sub>2</sub>/*h*-BN nanocomposites. The nomenclature of nanocomposites used in the legend is the same as in Table I, i.e., Ti/*h*-BN-1 and Ti/*h*-BN-2 denote Ti/*h*-BN nanocomposites milled in H<sub>2</sub>/He atmosphere for 66 and 206 min, respectively, while TiH<sub>2</sub>/*h*-BN denotes TiH<sub>2</sub> milled with *h*-BN additive for 66 min in pure He atmosphere. The ratio curve for pure Ti sample is shown in the figure as well.

erations in the sample. With prolonged milling time Ti particles transform into  $\delta$ -TiH<sub>1.95</sub> and Ti/*h*-BN nanocomposite milled for 206 min contains  $\delta$ -TiH<sub>1.95</sub> particles with mean size around 10 nm separated by *h*-BN in grains with diameter in the range 50–100 nm. Thus, size of Ti or  $\delta$ -TiH<sub>1.95</sub> particles in nanocomposites is significantly shorter than positron diffusion length [in metals typically 100–200 nm (Ref. 38)]. As a consequence, majority of positrons diffuse to *h*-BN additive and annihilates in a trapped state there. As discussed previously Ps formation occurs in *h*-BN (or B) additive only and Ps is localized in nanoscopic holes in the additives. Hence the contribution of Ps annihilations comes exclusively from the additive.

After prolonged milling for 206 min the Ti particles transform into  $\delta$ -TiH<sub>1.95</sub> particles with the mean size of 10 nm. Hence, similarly to the composite milled for 66 min, in the Ti/*h*-BN nanocomposite milled for 206 min most of positrons stopped in  $\delta$ -TiH<sub>1.95</sub> particles diffuse to *h*-BN additive and become trapped there. The increased contribution of positrons annihilated in the vicinity of Ti atoms observed in the composite milled for 206 min, see Fig. 10, indicates, therefore, that Ti atoms probably penetrate into the *h*-BN additive, i.e., to the vicinity of nanoscopic holes.

However, it is also clear from Fig. 10 that CDB ratio curves of Ti/*h*-BN nanocomposites cannot be fully explained only by contribution of positrons annihilated by Ti electrons. This is probably caused by a contribution of positrons annihilated by electrons belonging to H absorbed during milling from the effluent gas. This hypothesis will be discussed in the Sec. III E.

### D. TiH<sub>2</sub>/*h*-BN and TiH<sub>2</sub>/B nanocomposites

PL spectra of TiH<sub>2</sub> powder ball milled with *h*-BN or B additive in pure He atmosphere for 66 min can be again well-fitted by Eq. (4). The differences between TiH<sub>2</sub> and Ti-based nanocomposites can be summarized as follows:

- (i) TiH<sub>2</sub> based nanocomposites exhibit shorter o-Ps lifetime, i.e., smaller size of nanoscopic pores, than Ti-based nanocomposites milled for the same time;

- (ii) dispersion of the o-Ps lifetime in TiH<sub>2</sub>-based nanocomposites is larger than in Ti-based specimens, i.e., the size distribution of nanoscopic pores in TiH<sub>2</sub>-based nanocomposites is broader;
- (iii) TiH<sub>2</sub>-based nanocomposites exhibit significantly lower intensity of Ps component compared to Ti-based specimens. Hence, the probability of Ps formation in nanoscopic pores in TiH<sub>2</sub>-based nanocomposites is lower than in Ti-based specimens milled for the same time. However, similarly to Ti-based specimens TiH<sub>2</sub>/B nanocomposite contains lower concentration of nanoscopic pores than TiH<sub>2</sub>/*h*-BN.

The CDB ratio curve (related to pure *h*-BN) for TiH<sub>2</sub>/BN nanocomposite milled for 66 min is plotted in Fig. 10 together with the curves for Ti/*h*-BN nanocomposites. Clearly the shape of the ratio curve for TiH<sub>2</sub>/*h*-BN nanocomposite differs from that for Ti/*h*-BN specimen and also from that for pure Ti. This difference could be caused by a contribution of positrons annihilated by electrons, which belong to H. Hence the different shape of the CDB curve indicates that hydrogen in TiH<sub>2</sub>/*h*-BN nanocomposites fills the open volumes in *h*-BN structure.

Both PL and CDB results indicate that hydrogen contained in TiH<sub>2</sub> fills efficiently open volumes in TiH<sub>2</sub>/*h*-BN and TiH<sub>2</sub>/B nanocomposites. Hence, hydrogen is incorporated into free volumes more efficiently by milling of TiH<sub>2</sub> than by milling of Ti in H<sub>2</sub> atmosphere.

### E. Discussion of results

The PL measurements showed clearly that the size of nanoscopic pores in Ti/*h*-BN and Ti/B nanocomposites decreases with milling time. This is accompanied by a decrease in the probability of Ps formation reflected by a drop in intensity of the Ps component  $I_{Ps}$ . This effect can be explained by

- (i) an increased level of intermixing of Ti particles with *h*-BN (or B) additive, which leads to a reduction in pore sizes; and/or
- (ii) a filling of nanoscopic pores by hydrogen, which is absorbed in Ti/*h*-BN and Ti/B nanocomposites. Hydrogen may exist inside the nanoscopic pores either in form of H<sub>2</sub> molecules or absorbed on the inner surfaces of the pores.

The former effect is supported also by CDB results for Ti/*h*-BN nanocomposites shown in Fig. 10. The ratio curves for Ti/*h*-BN nanocomposites exhibit a peak centered at  $p \approx 13 \times 10^{-3} m_0c$  which increases with increasing milling time. This peak is very similar to the characteristic peak in pure Ti. Hence, this peak represents a contribution of positrons annihilated by Ti electrons and an increase in this peak with milling time reflects an increased level of intermixing of Ti and *h*-BN powders at nanoscopic scale, which leads to increasing number of Ti atoms in the vicinity of open volumes situated mostly in *h*-BN structure. However, one can see clearly in Fig. 10 that some features (especially the presence of a hump centered at  $p \approx 5 \times 10^{-3} m_0c$  and the ab-

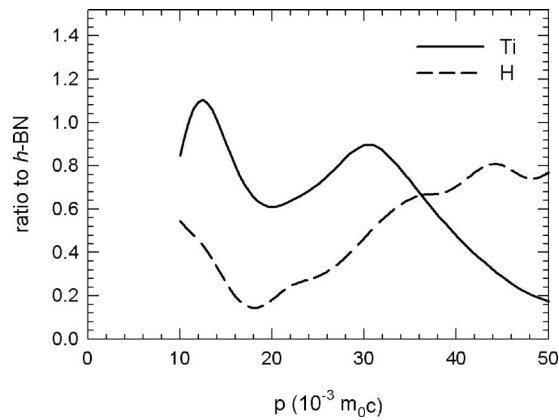


FIG. 11. HMP of ratio curves (related to pure *h*-BN) calculated for pure Ti (solid line) and a hypothetical case of *h*-BN lattice with B and N atoms replaced by hydrogen (dashed line).

sence of a broad peak at  $p \approx 30 \times 10^{-3} m_0c$ ) of CDB ratio curves for Ti/*h*-BN nanocomposites cannot be explained by annihilations with Ti-electrons. This result testifies that there is a significant fraction of positrons annihilated by electrons belonging to some other species. As the nanocomposites studied are known to contain hydrogen,<sup>36</sup> it is natural to attribute these additional features of CDB curves to a contribution of positrons annihilated by electrons belonging to hydrogen. Theoretical calculations of CDB curves were performed in order to estimate shape of the contribution of positrons annihilated by H electrons in Ti/*h*-BN nanocomposites. The high momentum parts (HMP) of CDB curves were calculated using ATSUP-based approach described in Ref. 39. The following core electron configurations were found to be in the best agreement with experiment and were used in the calculations of HMP curves:  $1s 2s 2p$  for B or N and [Ar] for Ti. The Doppler broadened CDB profiles were calculated for (i) pure *h*-BN, (ii) pure Ti, and (iii) a hypothetical case of *h*-BN lattice with B and N replaced by H atoms. Figure 11 shows the calculated HMP ratio curves (related to *h*-BN) for pure Ti and the case of *h*-BN lattice with H atoms. As valence electrons were not included in the calculations, it is meaningful to compare the calculated HMP curves with experiment only in the high momentum region  $p > 10 \times 10^{-3} m_0c$ , where annihilation with core electron dominates. One can see in Fig. 11 that despite a rather rough approach used the calculated HMP curve for pure Ti reproduces well the main features of experimental CDB curve, i.e., a sharp peak at  $p \approx 13 \times 10^{-3} m_0c$  and a wider peak centered at  $p \approx 30 \times 10^{-3} m_0c$ . The calculated curve for a pure contribution of positrons annihilated by H electrons increases at low momenta, see Fig. 11. This increase is in accordance with the peak observed on experimental curves at  $p \approx 5 \times 10^{-3} m_0c$  which was attributed to hydrogen.

Hence, CDB measurements support the picture that hydrogen fills the vacancy clusters and nanoscopic pores in Ti/*h*-BN nanocomposites. Taking into account PL and CDB results, we can conclude that the decrease in the lifetime  $\tau_d$  of positrons trapped at vacancy clusters and lifetime of the o-Ps component with milling time is likely caused by both factors mentioned in Sec. III C, i.e., (i) an increased intermixing of Ti and *h*-BN particles and also (ii) a filling of open

volumes by hydrogen. The Ti peak located at  $p \approx 13 \times 10^{-3} m_0c$  in CDB ratio curves is a measure of the level of intermixing of Ti and *h*-BN, while a hump at  $p \approx 5 \times 10^{-3} m_0c$  is most probably caused by hydrogen.

The effect of hydrogen can be clearly seen on CDB curves of TiH<sub>2</sub>/*h*-BN nanocomposites. Contrary to Ti/*h*-BN, milling of TiH<sub>2</sub>/*h*-BN nanocomposite was performed in He atmosphere, i.e., H is not absorbed from the gas phase but is already incorporated in TiH<sub>2</sub>. The shape of the CDB ratio curve measured on TiH<sub>2</sub>/*h*-BN nanocomposite at high momenta ( $p > 13 \times 10^{-3} m_0c$ ) is very similar to the curve of Ti/*h*-BN nanocomposite milled for the same time. Hence, the level of intermixing of TiH<sub>2</sub> and *h*-BN is similar as in Ti/*h*-BN. On the other hand, TiH<sub>2</sub>/*h*-BN nanocomposite exhibits remarkably higher hump at  $p \approx 5 \times 10^{-3} m_0c$  caused by hydrogen. This testifies that there is more hydrogen in the vicinity of open volume defects in TiH<sub>2</sub>/*h*-BN nanocomposite and filling of open volumes by hydrogen is reflected by

- (i) a reduced probability of Ps formation seen as a drop of  $I_{Ps}$ , see Fig. 4(c),
- (ii) a reduced lifetime  $\tau_{o-Ps}$  of the o-Ps component due to an enhanced electron density in the nanoscopic pores, see Fig. 4(a), and
- (iii) a reduced lifetime  $\tau_d$  of positrons trapped at vacancy clusters, see Fig. 3(a).

Interestingly, the size distribution of nanoscopic pores in TiH<sub>2</sub>/*h*-BN nanocomposite becomes broader, which could be due variations in local hydrogen concentration in various pores. TiH<sub>2</sub>/*h*-BN nanocomposite contains hydrogen dispersed on the atomic scale in TiH<sub>2</sub>. Thus, contrary to Ti/*h*-BN nanocomposites, TiH<sub>2</sub>/*h*-BN did not absorb H from the effluent gas because it was milled in a pure He atmosphere. It is likely that some Ti–H bonds break during the high-energy milling and the released H subsequently fills the open volumes. This is an important difference compared to Ti/*h*-BN nanocomposites because H is already inside the TiH<sub>2</sub> particles and its diffusion from the surface into bulk is not necessary. As a consequence, the filling of open volumes by hydrogen becomes more pronounced in TiH<sub>2</sub>-based nanocomposites.

XES investigations<sup>4</sup> of Ti/*h*-BN nanocomposites revealed that high-energy milling breaks some B–N bonds and N atoms are incorporated into Ti particles, which seem to have a positive impact on hydrogen uptake into Ti. The interstitial N atoms (probably associated with H in tetrahedral interstitial sites) are not detectable by PAS. However, the release of N atoms and their diffusion into Ti particles left N-vacancies in *h*-BN lattice. Isolated N-vacancies in *h*-BN are too shallow traps to be detected by PAS but if they agglomerate into larger clusters, they may contribute the longer component in PL spectra with lifetime  $\tau_d$ , which is attributed to positrons trapped at vacancy clusters. This process (i.e., diffusion of released N atoms into Ti and simultaneous formation of N-vacancies in *h*-BN) could be responsible for a slight increase in intensity  $I_d$  of this component with increasing milling time, which can be seen in Fig. 3(b).

Contrary to *h*-BN, the initial B powder does not contain any nanoscopic porosity. However, Ti/B nanocomposites contain nanoscopic porosity, which is testified by the formation of Ps. Hence, nanoscopic pores were created in Ti/B nanocomposites by high-energy milling. These pores could be situated at interfaces between Ti and B particles. After sufficiently long milling Ti/B nanocomposites exhibit nanoscopic pores with size distribution similar to that in Ti/*h*-BN despite the fact that initial powders are substantially different. One can see in Fig. 7 that Ti/B nanocomposite milled for 66 min exhibits size distribution of nanoscopic pores which is still narrower compared to that in Ti/*h*-BN. However, milling for 206 min is sufficient to achieve practically the same shape of distribution of nanoscopic porosity in Ti/B and Ti/*h*-BN nanocomposites. Nevertheless, the concentration of nanoscopic pores in Ti/B nanocomposites is lower than in Ti/*h*-BN as a rule. Figure 4 demonstrates that milling time has a similar effect to nanoscopic pores in Ti/B nanocomposites as in Ti/*h*-BN samples. Analogously to nanocomposites with *h*-BN additive, TiH<sub>2</sub>/B nanocomposite is characterized by a substantially reduced probability of Ps formation (i.e., a drop of  $I_{Ps}$ ) and a broader size distribution of nanoscopic pores. As was explained in the preceding paragraph, this is due to an enhanced effect of filling open volumes with hydrogen.

#### IV. CONCLUSIONS

Nanoscopic pores in Ti/*h*-BN and Ti/B nanocomposites prepared by high-energy ball milling were characterized by PAS. Size distribution of nanoscopic pores was calculated from the distribution of o-Ps lifetimes. It was found that the size of nanoscopic pores and also the probability of Ps formation decreases with increasing milling time. This is caused by factors: (i) an increased intermixing of Ti particles with *h*-BN or B additive on nanoscopic scale demonstrated by an increased concentration of Ti atoms in the vicinity of open volumes and (ii) the filling of nanoscopic pores with hydrogen. The presence of hydrogen in free volumes can be deduced from the shape of CDB ratio curves. It was demonstrated that hydrogen filling of nanoscopic pores is more pronounced in nanocomposites prepared by ball milling of TiH<sub>2</sub> with the additives. This testifies that some Ti–H bonds were broken during high-energy ball milling and hydrogen dispersed in TiH<sub>2</sub> on the atomic scale can diffuse quite easily to free volumes because contrary to hydrogen absorbed from effluent gas, there is no necessity to penetrate the surface barrier. Sufficiently long milling time leads to very similar size distribution of nanoscopic pores Ti/*h*-BN and Ti/B nanocomposites. However, the concentration of nanoscopic pores in Ti/B nanocomposites is lower as a rule.

#### ACKNOWLEDGMENTS

This work was supported by The Ministry of Education, Youth, and Sports of The Czech Republic (Project Nos. MS 0021620834 and MEB100912), The Academy of Science of

Czech Republic (Project No. KAN300100801), INTAS (Project No. 05-100005-7672), RFBR (Project No. 07-03-00610), and The Alexander von Humboldt Foundation.

- <sup>1</sup>H. Zhang and E. H. Kisi, *J. Phys.: Condens. Matter* **9**, L185 (1997).
- <sup>2</sup>J.-L. Bobet, C. Even, and J.-M. Quenisset, *J. Alloys Compd.* **348**, 247 (2003).
- <sup>3</sup>T. Mütschele and R. Kirchheim, *Scr. Mater.* **21**, 1101 (1987).
- <sup>4</sup>C. Borchers, A. V. Leonov, T. I. Khomenko, and O. S. Morozova, *J. Phys. Chem. B* **109**, 10341 (2005).
- <sup>5</sup>A. Zaluska, L. Zaluski, and J. O. Ström-Olsen, *J. Alloys Compd.* **288**, 217 (1999).
- <sup>6</sup>G. Liang, S. Boily, J. Huot, A. Van Neste, and R. Schulz, *J. Alloys Compd.* **267**, 302 (1998).
- <sup>7</sup>H. Imamura, Y. Takesue, S. Tabata, N. Shigetomi, Y. Sakata, and S. Tsuchiya, *Chem. Commun. (Cambridge)* **22**, 2277 (1999).
- <sup>8</sup>C. Z. Wu, P. Wang, X. Xiao, C. Liu, D. M. Chen, G. Q. Lu, and H. M. Cheng, *J. Alloys Compd.* **414**, 259 (2006).
- <sup>9</sup>C. Borchers, O. S. Morozova, T. I. Khomenko, A. V. Leonov, A. V. Postnikov, E. Z. Kurmaev, A. Moewes, and A. Pundt, *J. Phys. Chem. B* **110**, 196 (2006).
- <sup>10</sup>C. Borchers, O. S. Morozova, T. I. Khomenko, A. V. Leonov, E. Z. Kurmaev, A. Moewes, and A. Pundt, *Chem. Phys. Lett.* **465**, 82 (2008).
- <sup>11</sup>Y. C. Jean, in *Proc. Int. School of Physics "Enrico Fermi," Course CXXV*, edited by A. Dupasquier and A. P. Mills (IOS, Varenna, 1995) p. 563.
- <sup>12</sup>S. J. Tao, *Appl. Phys. (Berlin)* **10**, 67 (1976).
- <sup>13</sup>O. E. Mogensen, *Positron Annihilation in Chemistry* (Springer-Verlag, Berlin, 1995).
- <sup>14</sup>S. J. Tao, *J. Chem. Phys.* **56**, 5499 (1972).
- <sup>15</sup>M. Eldrup, D. Lightbody, and J. N. Sherwood, *J. Chem. Phys.* **63**, 51 (1981).
- <sup>16</sup>H. Nakanishi, S. J. Wang, and Y. C. Jean, in *Positron Annihilation Studies of Fluids*, edited by S. C. Sharma (World Scientific, Singapore, 1988), p. 292.
- <sup>17</sup>F. Bečvář, J. Čížek, I. Procházka, and J. Janotová, *Nucl. Instrum. Methods Phys. Res. A* **539**, 372 (2005).
- <sup>18</sup>F. Bečvář, J. Čížek, and I. Procházka, *Appl. Surf. Sci.* **255**, 111 (2008).
- <sup>19</sup>F. Bečvář, *Nucl. Instrum. Methods Phys. Res. B* **261**, 871 (2007).
- <sup>20</sup>J. Kansy, *Nucl. Instrum. Methods Phys. Res. A* **374**, 235 (1996).
- <sup>21</sup>J. Čížek, I. Procházka, B. Smola, I. Stulíková, R. Kužel, Z. Matěj, and V. Cherkaska, *Phys. Status Solidi A* **203**, 466 (2006).
- <sup>22</sup>M. J. Puska and R. M. Nieminen, *J. Phys. F: Met. Phys.* **13**, 333 (1983).
- <sup>23</sup>E. Boroński and R. M. Nieminen, *Phys. Rev. B* **34**, 3820 (1986).
- <sup>24</sup>M. J. Puska, S. Mäkinen, M. Manninen, and R. M. Nieminen, *Phys. Rev. B* **39**, 7666 (1989).
- <sup>25</sup>R. Geick, C. H. Perry, and G. Rupprecht, *Phys. Rev.* **146**, 543 (1966).
- <sup>26</sup>O. Madelung, U. Rössler, and M. Schulz, *Non-Tetrahedrally Bonded Elements and Binary Compounds I*, Landolt-Börnstein-Group III, Condensed Matter (Springer-Verlag, Berlin, 2006), Vol. 41C, p. 463.
- <sup>27</sup>R. R. Pawar and V. T. Deshpande, *Acta Crystallogr.* **24A**, 316 (1968).
- <sup>28</sup>JCPDS file number 73–2095, JCPDS International Center for Diffraction Data.
- <sup>29</sup>L. McCarty, *J. Am. Chem. Soc.* **50**, 2562 (1958).
- <sup>30</sup>J. M. Campillo Robles, E. Ogando, and F. Plazaola, *J. Phys.: Condens. Matter* **19**, 176222 (2007).
- <sup>31</sup>P. K. Pujari, K. Sudarshan, A. Goswami, S. B. Manohar, D. K. Aswal, A. Singh, S. Sen, and S. K. Gupta, *Phys. Rev. B* **66**, 012518 (2002).
- <sup>32</sup>K. Hirata, Y. Kobayashi, and Y. Ujihira, *J. Chem. Soc., Faraday Trans.* **92**, 985 (1996).
- <sup>33</sup>R. L. deZafra, *Phys. Rev.* **113**, 1547 (1959).
- <sup>34</sup>J. Kansy, *Acta Phys. Pol. A* **113**, 1397 (2008).
- <sup>35</sup>R. West, in *Positrons in Solids*, edited by P. Hautojärvi (Springer-Verlag, Berlin, 1979), p. 89.
- <sup>36</sup>H. Murakami and T. Endo, *J. Phys.: Condens. Matter* **1**, SA131 (1989).
- <sup>37</sup>C. Borchers, O. S. Morozova, T. I. Khomenko, A. V. Leonov, A. V. Postnikov, E. Z. Kurmaev, A. Moewes, and A. Pundt, *J. Phys. Chem. C* **112**, 5869 (2008).
- <sup>38</sup>M. J. Puska and R. M. Nieminen, *Rev. Mod. Phys.* **66**, 841 (1994).
- <sup>39</sup>J. Kuriplach, A. L. Morales, C. Dauwe, D. Segers, and M. Šob, *Phys. Rev. B* **58**, 10475 (1998).